

Depth resolution of transmission ERDA for H in Al under nuclear-elastically enhanced recoiling of H by 8 MeV He

H. Kudo¹ * , H. Naramoto¹, M. Sataka¹, S. Ishii¹, K. Sasa^{1,2}, S. Tomita²

¹*Research Facility Center for Science and Technology, University of Tsukuba, 1-1-1 Tennodai, Tsukuba, Ibaraki 305-8577, Japan*

²*Faculty of Pure and Applied Sciences, University of Tsukuba, 1-1-1 Tennodai, Tsukuba, Ibaraki 305-8571, Japan*

ABSTRACT

Using stacked samples of Al foil and H-containing resin film, we have carried out elastic recoil detection analysis with transmission layout (T-ERDA) to investigate the depth resolution in the measurements of H distribution in Al. For narrow and wide acceptance conditions of the detector, the depth resolutions of 1.5–4.9 μm at several depths in Al of 50 and 80 μm thicknesses have been determined for incidence of 8 MeV ^4He . While the main factor to degrade the depth resolution is the energy straggling of recoil H for narrow acceptance conditions, it is the smearing of the low-energy side of H spectrum due to the angular spread of H for wide acceptance conditions. The knowledge obtained in this work is useful for analysis of 3D images of H distribution measured by T-ERDA, for example, future analysis of minerals or natural glass samples to determine abundances and distributions of water or OH in the samples.

*Corresponding author *E-mail address*: kudo@tac.tsukuba.ac.jp

I Introduction

We have recently developed a non-destructive observation technique of hydrogen distribution in matter by applying elastic recoil detection analysis with transmission layout (T-ERDA) [1]. Actually, 3D distribution of hydrogen bubbles of ten- μm size in Al was visualized by T-ERDA using a micro-beam. In this case, an 8 MeV $^4\text{He}^{2+}$ beam collimated to a $\sim 3\text{-}\mu\text{m}$ size was used to scan the surface of H-charged Al. The recoil H resulting from hard collisions with He was energy-analyzed in the direction close to 0° after passing through the sample, thereby depth distribution of hydrogen was determined by energy-to-depth conversion using the known stopping powers.

Under such experimental conditions, the recoil cross section as large as $\sim 2\text{ b/sr}$ due to the nuclear elastic interaction of 8 MeV ^4He with H leads to sufficient count rate of recoil H [2] [3], which allows 3D mapping of H using a collimated weak beam of the μm size. A remarkable advantage of T-ERDA is the direct detection of hydrogen in a material with a higher spatial resolution than for the typical case of neutron tomography [4]. This is in contrast to other observation techniques such as electron microscopy (TEM, SEM) or X-ray tomography, from which information obtained is hydrogen-induced structural changes of the base material since these techniques are insensitive to hydrogen itself.

From a different standpoint, geological samples typically contain H in the form of water (H_2O) or hydroxyls (OH), hence analysis of H is of scientific as well as technical interest. Indeed, several workers used ERDA or related techniques to detect hydrogen in minerals [5] [6] [7] [8] [9] [10]. When T-ERDA is used to observe H in precipitates or inclusions contained in the sample, the local stopping power associated with the local atomic composition must be used in the energy-to-depth conversion. This means that we can expect to determine the local atomic composition, i.e., the atom species existing around H. The 3D images of H-containing aggregates with more than ten μm size in minerals or natural glass samples possibly allow to determine abundances and distributions of water or OH in the samples. Furthermore, such analysis is of geological importance since it is certainly helpful to discuss the origin of the lunar water and the earth's sea via hydrogen analyses of glasses and minerals in lunar rocks [11] [12].

With the scientific and technical background mentioned above, refinement of the T-

ERDA technique is required to obtain detailed knowledge about the state or behavior of hydrogen in matter. For this purpose, we have experimentally determined depth resolutions for analysis of H distribution in Al. These data are also useful not only when Al is employed as a stopping foil for T-ERDA of thin samples, but also when we need to estimate spatial resolutions for H in other materials including mineral samples by scaling with stopping powers.

II Experiments

In the present experiments, Al foils and PPS [polyphenylene sulfide $(C_6H_4S)_n$] films were stacked and used for test samples. The thicknesses of Al and PPS were determined by measuring their weight and area, assuming the densities of 2.70 and 1.35 g/cm³ for Al and PPS, respectively. The measurement reproduced the nominal Al thicknesses of 5–80 μm within $\pm 2\%$. The measured PPS thickness is $1.35 \pm 0.05 \mu\text{m}$, which is thin enough to use as a hydrogen marker. We have prepared 7 samples, S-1 to S-7, by stacking these Al foils and PPS films. Their details are listed in Table 1, together with the experimental data. It is notable that the total thicknesses of Al in the samples are more than 50 μm to prevent He from entering the detector, taken into account the 43 μm range of 8 MeV He in Al.

The experimental setup and procedure are similar to the previous case [1]. A particle detector for energy analysis of H was set on the ion-beam axis and a sample was placed in front of the detector. The acceptance angular range of the detector, being expressed as 0 to ϕ_m polar angle with respect to the beam axis, was adjusted by attaching a circular aperture on the detector. In the present experiments, we have chosen $\phi_m = 4.1^\circ$ for narrow and 11.1° for wide typical acceptance conditions using the apertures of 2.0 and 5.5 mm diameter, respectively. These are typical conditions chosen to obtain sufficient count rate of recoil H, depending on the H concentration in the sample.

The recoil cross section for hard collision of ^4He with ^1H has a maximum at the incident He energy of 8–10 MeV [2] [3]. In this energy range, the stopping powers of matter with low atomic number such as Al decrease with increasing the He energy. This is also the case for recoil H in the MeV energy range. The depth resolution relying on the ion's energy

loss degrades with decreasing stopping powers, namely with increasing the incident He energy in the 8–10 MeV range. Therefore, we have chosen 8 MeV ${}^4\text{He}^{2+}$ energy to obtain relatively high count rate and high depth resolutions. In the measurements, the beam current was ~ 100 pA for a beam spot of $\sim 50 \times 50 \mu\text{m}^2$, which allowed 5–10 min. for accumulating a spectrum. The energy-measuring system for H was calibrated with 5.48 MeV α particles emitted from ${}^{241}\text{Am}$, together with a test pulser. The energy resolution of the measuring system including the particle detector was 32 keV.

III Results and discussion

It is of fundamental importance to confirm the applicability of a straight-path picture for the He and H trajectories in the present experimental conditions of T-ERDA. Figure 1 shows angular spreads of incident 8 MeV He and recoil H in the Al sample of $80 \mu\text{m}$ thickness, which were obtained by TRIM simulations [13]. The angular spread of He in Al is as small as 0.95° from the beam axis at the depth of $10 \mu\text{m}$, which is the maximum analyzing depth of interest for typical use of the present T-ERDA. This depth is sufficiently shallower than the detection limit of $30 \mu\text{m}$ depth, corresponding to zero energy of H after passing through the Al sample. The above angular spread causes uncertainty in the lateral direction of $10 \times 2 \tan 0.95^\circ = 0.33 \mu\text{m}$, which is much smaller than the typical beam size of $\sim 3 \mu\text{m}$ used for 3D mapping. Therefore, the lateral resolution at least up to the $10 \mu\text{m}$ depth remains approximately equal to the beam size. Meanwhile, most of recoil H starting from the Al surface in the 0° direction spread over a narrow angular range of 0 – 2.3° from the beam axis after passing through the Al foil.

The straight-path picture confirmed above is applied to the motions of the projectile He, which is incident perpendicularly on the Al surface, and recoil H with a recoil angle ϕ ($0 \leq \phi < \pi/2$) from the beam axis. In this case, the energy E of recoil H measured after passing through the Al sample can be converted to the depth z where H recoil occurs, i.e.,

$$E = \alpha \cos^2 \phi \left(\mathcal{E}_{\text{inc}} - \int_0^z S_{\text{He}} dz \right) - \int_z^{L/\cos \phi} S_{\text{H}} dz, \quad (1)$$

where $\alpha = 4M_{\text{H}}M_{\text{He}}/(M_{\text{H}} + M_{\text{He}})^2 = 0.64$ with M_{H} and M_{He} being the atomic masses of

H and He, respectively, $\mathcal{E}_{\text{inc}} = 8 \text{ MeV}$ is the energy of incident He in the present case, L is the thickness of the Al sample, S_{He} and S_{H} are the stopping powers of Al for He and H, respectively. The first term on the right side of Eq. (1) represents the energy of recoil H produced at z , while the second represents the energy loss of H in the outgoing path. In the following analysis, the values of stopping powers were obtained from the SRIM tables [13].

Figure 2 shows energy spectra of H measured under the narrow acceptance conditions ($\phi_{\text{m}} = 4.1^\circ$) for S-1 to S-3 samples of Al/PPS/Al(50 μm thickness). The thicknesses of the top Al layers are 0, 10, and 20 μm for S-1, S-2, and S-3, respectively. For convenience of analysis, the yields have been scaled to have the same peak height as of S-1. We see sharp peaks originating from hydrogen in the PPS film. The three peaks are slightly asymmetric, which can be recognized by the larger number of plots (equally spaced with respect to H energy) on the left side than on the right side, indicating the existence of low-energy tails. The peak energies can be accounted for with the depth scales indicated in Fig. 2, which were drawn with Eq. (1) for $\phi = 0$. For the three cases, however, we see slight shift of the peak energy to the low-energy side from the scale. Such peak shift arises from the finite thickness of the PPS film. Since for both the incident He and recoil H, the ratio of PPS to Al stopping power is 0.64, the effective thickness of PPS measured on the Al depth scale is $1.35 \times 0.64 = 0.86 \mu\text{m}$. Accordingly, we may expect the peak shift equal to the half thickness of $0.43 \mu\text{m}$ and thereby the observed peak shifts can be explained. In Fig. 2, the dashed curve shows the calculated spectrum by TRIM for 0-degree recoil of H starting from the surface of 50- μm thick Al. The peak energy of 4.31 MeV by TRIM coincides with the origin of the depth scale indicated by using Eq. (1) for $\phi = 0$. About 60% of the experimental FWHM value of 0.130 MeV corresponds to the TRIM value of 0.081 MeV which is due to energy straggling.

Figure 3 shows energy spectra of H measured under wide acceptance conditions ($\phi_{\text{m}} = 11.1^\circ$) for S-4 to S-7 samples of Al/PPS/Al, in which H yields are shown for the same number of incident He. Low-energy tails are more discernible than those in Fig. 2. We also see low-energy shift of the H peak from the depth scale, which is due to the PPS thickness, as already discussed for the case of narrow acceptance. In Fig. 3, the dashed curve shows the calculated spectrum by TRIM for 0-degree recoil of H starting from the

Table 1: Names and structures of the samples, peak energies of H from the PPS layer in Al, FWHM values of the H peak, and the depth resolutions Δz determined after correction of the PPS thickness ($1.35 \mu\text{m}$) to the FWHM values. S-1 to S-3 are the test samples for the narrow acceptance of the detector ($\phi_m = 4.1^\circ$), while S-4 to S-7 for the wide acceptance ($\phi_m = 11.1^\circ$). The uncertainty in the values of Δz is $\pm 2.5\%$.

Sample name and structure	Peak energy (MeV)	FWHM (MeV)	FWHM (μm)	Δz (μm)
S-1: PPS/Al($50 \mu\text{m}$)	4.25	0.130	1.81	1.59
S-2: Al($10 \mu\text{m}$)/PPS/Al($50 \mu\text{m}$)	3.31	0.160	1.78	1.56
S-3: Al($20 \mu\text{m}$)/PPS/Al($50 \mu\text{m}$)	2.14	0.202	1.68	1.45
S-4: PPS/Al($80 \mu\text{m}$)	3.72	0.400	4.94	4.86
S-5: Al($5 \mu\text{m}$)/PPS/Al($75 \mu\text{m}$)	3.30	0.408	4.70	4.62
S-6: Al($10 \mu\text{m}$)/PPS/Al($70 \mu\text{m}$)	2.86	0.433	4.47	4.39
S-7: Al($15 \mu\text{m}$)/PPS/Al($65 \mu\text{m}$)	2.34	0.480	4.40	4.32

surface of $80\text{-}\mu\text{m}$ thick Al (for the case shown in red in Fig. 1). Again, the peak energy of 3.77 MeV by TRIM coincides with the origin of the depth scale given by using Eq. (1) for $\phi = 0$. The difference between the experimental FWHM value of 0.400 MeV for S-4 and the TRIM value of 0.109 MeV is of essential interest in the following analysis.

The measured FWHM values of H peaks for samples S-1 to S-7 are summarized in Table 1. The FWHM values in MeV have been converted to those in μm , by applying the depth scales indicated in Figs. 2 and 3. In Table 1, the depth resolutions Δz have been estimated by subtracting the effect of PPS thickness by assuming the convolution characteristic of Gaussian distributions, i.e., $\Delta z = (1.81^2 - 0.86^2)^{1/2} = 1.59 \mu\text{m}$ for S-1, for example. For S-4, the calculated value of mean energy spread 0.109 MeV due to energy straggling, noted earlier, corresponds to the depth uncertainty of $1.33 \mu\text{m}$, which might be the best depth resolution that can be reached in this case.

For S-1 to S-3 in Table 1, FWHM (MeV) increases with increasing the thickness of Al foil on PPS, whereas FWHM (μm) and Δz decrease oppositely. Similar opposite dependences are also seen for S-4 to S-7. Such behavior is expected to occur for two reasons. First, the stopping powers of Al for both the incident He and recoil H increase

as they lose energy in Al, which extends the depth scale with increasing depth. Second, the peak widths are predominantly determined by a different factor from the energy-loss process, which will be discussed later, otherwise the peak width should increase proportionally to the depth scale. Such feature of T-ERDA simplifies understanding of 3D images of H distributions because the depth resolution does not degrade with increasing depth, but it rather remains approximately constant in the depth range of interest, as is seen in Table 1.

To understand the origin of low-energy tails of H peaks appearing remarkably under the wide acceptance conditions, we need to follow the processes of recoil and energy loss. Usually, the recoil cross section $d\sigma/d\Omega$ is written as a function of ϕ . By variable transformation from ϕ to the recoil H energy T using the relation

$$T = \alpha \mathcal{E}_{\text{inc}} \cos^2 \phi, \quad (2)$$

the recoil cross section $d\sigma/dT$, which represents the initial energy distribution of recoil H, is expressed as

$$\frac{d\sigma}{dT} = \frac{d\sigma}{d\Omega} \frac{d\Omega}{dT} = \frac{d\sigma}{d\Omega} \frac{\pi}{\sqrt{\alpha \mathcal{E}_{\text{inc}} T}}, \quad (3)$$

where $d\Omega = 2\pi \sin \phi d\phi$. Figure 4 shows $d\sigma/dT$ calculated from Eq. (3) using $d\sigma/d\Omega$ given by SigmaCalc data [14], together with that for Coulomb interaction only, i.e., for the case of Rutherford scattering. The energy ranges which correspond to the angular acceptance range of the detector, under the straight-path assumption, are shown by arrows. From Eq. (3), the observed H-energy spectrum is given by

$$\frac{d\sigma}{dE} = \frac{d\sigma}{dT} \frac{dT}{dE}. \quad (4)$$

For Al of 80 μm thickness, $dT/dE = 0.68$ in the ranges of T and E in consideration is obtained numerically using Eq. (1). The calculated $d\sigma/dE$ for the case of S-4 ($z = 0$, $\phi_m = 11.1^\circ$, and $L = 80 \mu\text{m}$) is shown in Fig. 5.

High- and low-energy sides of the H peak originate from the energy signals generated from the central and peripheral area of the detector window (5.5 mm diameter for S-4,

as noted in §II), respectively. This is evident from the two spectra for S-4, shown in Fig. 5, which were measured for the same number of incident He (1.4×10^{11}). As the beam spot was moved from the center to the edge of the sample mounted on the sample holder, the tail on the low-energy side reduced drastically, as seen in Fig. 5. This is because the peripheral area of the detector window is partly in the shadow of the sample holder, preventing low-energy H in the shadow from entering the detector. It should be noted that the tail of the spectrum for the center, shown in blue in Fig. 5, is slightly higher than the corresponding spectrum for S-4 in Fig. 3, although the FWHM values obtained from these different runs are approximately the same. This demonstrates sensitive dependence of the tail on the experimental conditions, for example, a possible deviation of the center of the detector from the beam axis. Considering the above correspondence between the H energy and the position on the detector window, the low-energy side of the H peak should be smeared considerably by the angular spread of recoil H during passage in Al, in contrast to the high-energy side. This causes the low-energy tail, giving rise to the asymmetric triangular spectrum.

In the following, the representative cases for S-1 and S-4 are discussed since general aspects of the peak width can be deduced from these two cases. According to calculations with known stopping powers, the range of $5.094 \leq T \text{ (MeV)} \leq 5.120$ for the narrow acceptance leads to $4.277 \leq E \text{ (MeV)} \leq 4.309$ after passing through Al of $50 \mu\text{m}$ thickness. Similarly, $4.93 \leq T \text{ (MeV)} \leq 5.12$ for the wide acceptance leads to $3.49 \leq E \text{ (MeV)} \leq 3.77$ after passing through Al of $80 \mu\text{m}$ thickness. The widths of these E ranges, 0.032 and 0.28 MeV, can be increased and smeared by two intrinsic factors. One is the energy straggling of H in Al, which is recognized as the FWHM peak widths of the TRIM spectra, 0.081 and 0.109 MeV in Figs. 2 and 3, respectively. Another factor is the counting of low-energy recoil H with a recoil angle greater than ϕ_m , that can enter the detector after being deflected towards the detector. Actually, the FWHM angular spreads of H after passing through Al of 50 and $80 \mu\text{m}$ thicknesses are 1.2 and 2.3° from the beam axis, respectively. This means that the low-energy ends of the T ranges noted above should be replaced by the convoluted values of $(4.1^2 + 1.2^2)^{1/2} = 4.3^\circ$, and by $(11.1^2 + 2.3^2)^{1/2} = 11.3^\circ$ for the narrow and wide acceptance, respectively. These values lower the low-energy ends of the T ranges noted above, providing the modified widths of E ranges, 0.035 and 0.32

MeV, instead of 0.032 and 0.28 MeV, for the narrow and wide acceptance, respectively. We again apply the convolution characteristic to the four energy widths, i.e., the energy acceptance, the width due to energy straggling, the energy resolution of the detector system 0.032 MeV, and the energy loss of H during passage through the PPS layer 0.013 MeV, although the last one makes little contribution to the results. Finally, we obtain the energy widths of $\Delta E = (0.035^2 + 0.081^2 + 0.032^2 + 0.013^2)^{1/2} = 0.095$ and $(0.32^2 + 0.109^2 + 0.032^2 + 0.013^2)^{1/2} = 0.34$ MeV for the narrow and wide acceptance, respectively. These values are 73 and 85% of the experimental values of 0.130 and 0.400 MeV for S-1 and S-4 samples, respectively. Such fair agreement between the experimental and calculated values is rather satisfactory, considering the crudeness of the present analysis. From the above discussion, the following conclusion is obtained. For narrow acceptance conditions, the main factor to degrade the energy resolution, and therefore, the depth resolution is the energy straggling of H in Al. As the angular acceptance of the detector increases, the low-energy side of the spectrum extends to form a tail, while the high-energy side remains unchanged. This causes the degraded depth resolution corresponding to the deformed triangular spectrum.

In relation to the spectrum shape, it is notable to compare the present nuclear elastic condition with the Rutherford case, shown in Fig. 4. In addition to the extremely larger cross section than the Rutherford case, there is a noticeable difference between the two. Indeed, $d\sigma/dT$ in the present case decreases with decreasing T , while it increases as $d\sigma/dT \propto T^{-2}$ in the Rutherford case. Accordingly, the high-energy recoil more contributes to the high energy side of the H peak in the nuclear elastic case than in the Rutherford case. This certainly causes sharp high-energy side of the H peak in the nuclear elastic condition.

In the previous work under wide acceptance conditions of 15.3° , we reported that the depth resolution of $\sim 1.2 \mu\text{m}$ was estimated using the high-energy edge of the H image [1], without noticing the long tail that must be hidden under the H image. Therefore, the above value must be corrected to a larger value of more than $4.86 \mu\text{m}$ for S-4 under the present definition of the depth resolution. However, the spectrum shape having a long tail cannot be fully characterized only by its FWHM value. The contrast of 3D image, like those reported previously, might be more suitably understood with the sharpness

of high-energy edge of the image rather than with the FWHM value. Thus, the depth resolution in T-ERDA should be properly defined, depending on the observed image of interest.

IV Conclusion

The feature of the depth resolution in T-ERDA has been studied for a better understanding of 3D images of H distribution in matter. The main degrading factor for the depth resolution is the energy straggling of H in Al for narrow acceptance conditions of the detector. As the acceptance angle of the detector increases, the low-energy side of recoil H spectrum extends to form a tail, while the sharp high-energy side remains unchanged. It follows that the depth resolution is degraded by the enhanced FWHM value of the deformed triangular spectrum.

In T-ERDA using a micro-beam, 3D images of H distributions in a local structure in the sample can be obtained by energy-to-depth conversion using the local stopping power associated with the local atomic composition. Therefore, such 3D images possibly inform us of the atom species existing around H in the sample. 3D images of H-containing aggregates possibly allow, for example, to identify abundances and distributions of water or OH in minerals and natural glass samples, based on the knowledge about depth resolutions obtained in the present work. For such analysis, simultaneous measurements of characteristic x-rays induced by the He beam will be helpful [2].

ACKNOWLEDGEMENTS

The authors thank the technical staff of UTTAC for operating the 6MV tandem accelerator, and thank G. Kawasaki and S. Hatada for their support during experiments. We also thank Dr. M. Kurosawa for valuable comments for the manuscript. We are grateful to Toray KP Films Inc. for providing the PPS films, and to Toyo Aluminium K.K. for providing the high-purity Al foils. This work was developed partly from the experimental research program supported by Cross-Ministerial Strategic Innovation Promotion Program – Unit D66 –Innovative measurement and analysis for structural materials (SIP-IMASM) operated by the Japanese cabinet office.

References

- [1] A. Yamazaki, K. Sasa, S. Tomita, S. Ishii, H. Naramoto, M. Sataka, H. Kudo, G. Itoh, M. Ohkubo, *AIP Advances* 9 (2019) 105111.
- [2] A. Yamazaki, H. Naramoto, K. Sasa, S. Ishii, S. Tomita, M. Sataka, H. Kudo, M. Ohkubo, A. Uedono, *Nucl. Instrum. Meth. Phys. Res. B* 450 (2019) 319.
- [3] IBANDL (Ion Beam Analysis Nuclear Data Library). <https://www-nds.iaea.org/exfor/ibandl.htm>.
- [4] A. Griesche, E. Dabah, T. Kannengiesser, N. Kardjilov, A. Hilger, I. Manke, *Acta Materialia* 78 (2014) 14.
- [5] R. J. Sweeney, V. M. Prozesky, K. A. Springhorn, *Geochim. Cosmochim. Acta* 61 (1997) 101.
- [6] K. Furuno, T. Komatsubara, K. Sasa, H. Oshima, Y. Yamato, S. Ishii, H. Kimura, M. Kurosawa, *Nucl. Instrum. Meth. Phys. Res. B* 210 (2003) 459.
- [7] T. Komatsubara, K. Sasa, K. Okumoto, S. Ishii, Y. Yamato, K. Satou, K. Furuno, M. Kurosawa, *Nucl. Instrum. Meth. Phys. Res. B* 251 (2006) 237.
- [8] C. Raepsaet, H. Bureau, H. Khodja, A. Aubaud, A. Carraro, *Nucl. Instrum. Meth. Phys. Res. B* 266 (2008) 1333.
- [9] H. Bureau, C. Raepsaet, H. Khodja, A. Carraro, C. Aubaud, *Geochim. Cosmochim. Acta* 73 (2009) 3311.
- [10] F. A. Weis, L. Ros, P. Reichart, H. Skogby, P. Kristiansson, G. Dollinger, *Phys. Chem. Miner.* 45 (2018) 669.
- [11] A. Stephant, M. Anand, H. Ashcroft, X. Zhao, S. Huc, R. Korotev, S. Strekopytov, R. Greenwood, E. Humphreys-Williams, Y. Liu, G. Tang, Q. Li, I. Franchi, *Geochim. Cosmochim. Acta* 266 (2019) 163.
- [12] Y. Lina, W. van Westrenen, *Global Planet. Change* 197 (2021) 103393.

[13] J. F. Ziegler, J. P. Biersack, SRIM2013, The Stopping and Range of Ions in Matter.
<http://www.srim.org/>

[14] A. F. Gurbich, Nucl. Instrum. Meth. Phys. Res. B 371 (2016) 27.

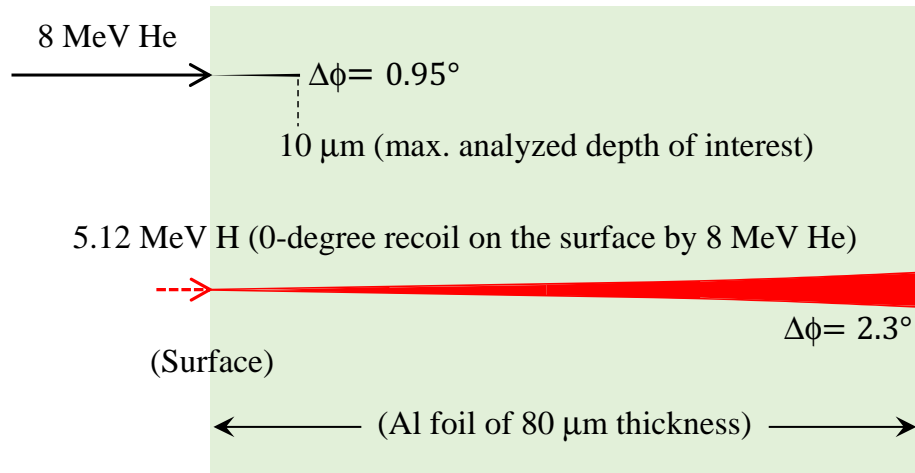


Figure 1: Angular spreads $\Delta\phi$ calculated with TRIM for 8 MeV He and 5.12 MeV H (shown in red) incident on the Al foil of $80\ \mu\text{m}$ thickness. The latter results from head-on collision of 8 MeV He with H on the surface. For the Al foil of $50\ \mu\text{m}$ thickness, $\Delta\phi = 1.2^\circ$ on the back surface.

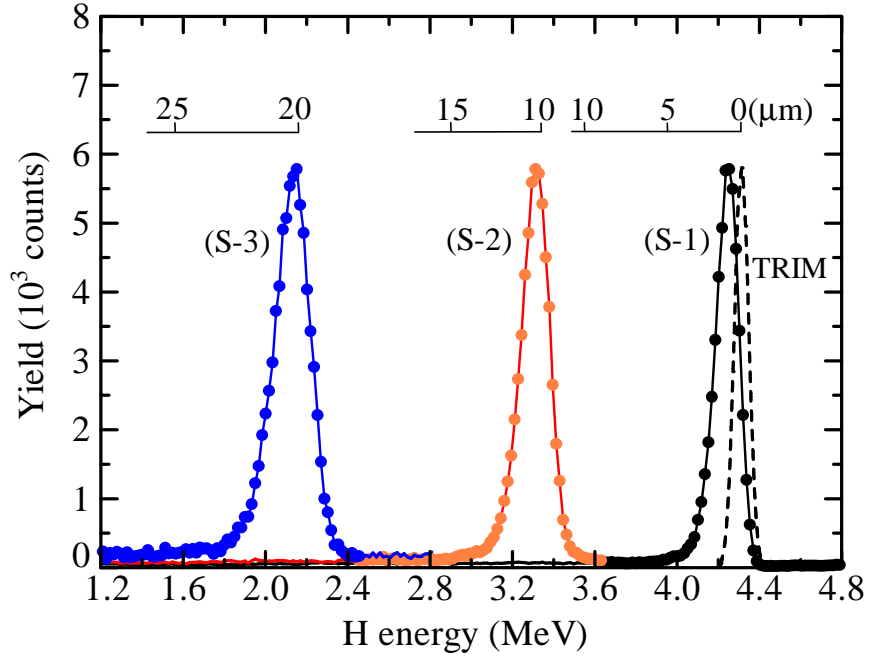


Figure 2: T-ERDA spectra of H measured for S-1 to S-3 samples of Al/PPS/Al with the narrow acceptance of $\phi_m = 4.1^\circ$. The spectra have been scaled to have the same peak height. The depth scales based on the straight-path model, given by Eq. (1) for $\phi = 0$, are indicated for the three cases. The calculated spectrum using TRIM for 0-degree recoil is also shown with the same peak height for comparison of the peak width.

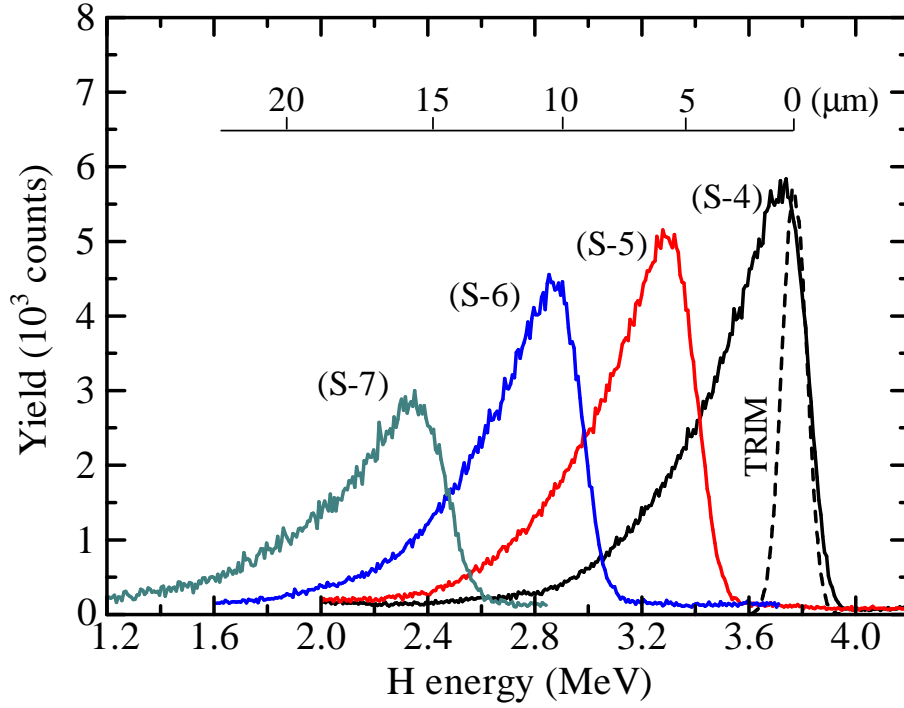


Figure 3: T-ERDA spectra of H measured for S-4 to S-7 samples of Al/PPS/Al with the wide acceptance of $\phi_m = 11.1^\circ$. The spectra are shown for the same number of incident He. The depth scale for Al based on the straight-path model, given by Eq. (1) for $\phi = 0$, is indicated. The calculated spectrum using TRIM for 0-degree recoil (for the case shown in red in Fig. 1) is also shown with the same peak height as of S-4 for comparison of the peak width.

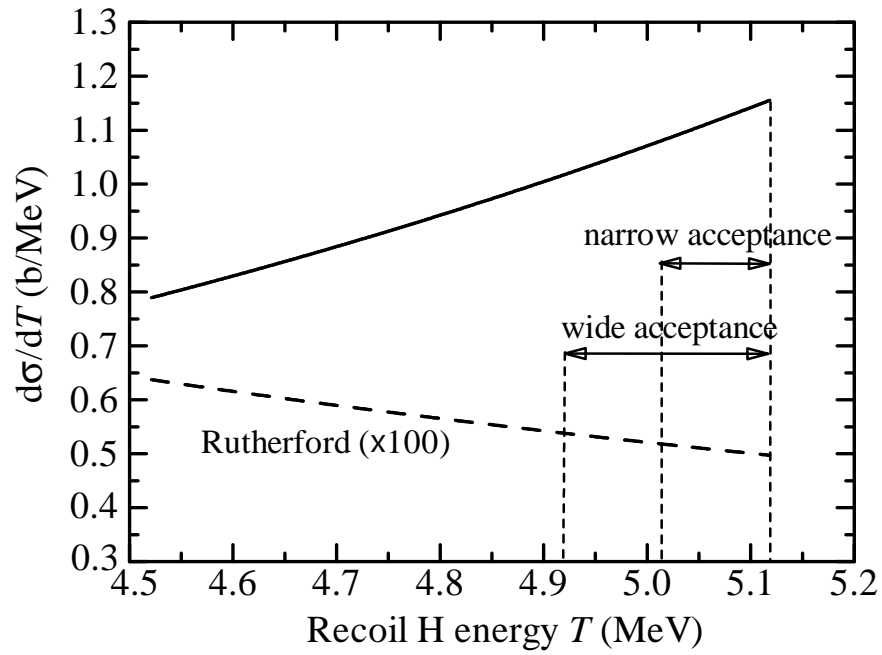


Figure 4: Recoil cross section as a function of recoil H energy, representing the initial energy spectrum of recoil H. The dashed curve shows the Rutherford case (Coulomb interaction only) for comparison. The energy ranges corresponding to the narrow ($\phi_m = 4.1^\circ$) and wide ($\phi_m = 11.1^\circ$) acceptance conditions are indicated.

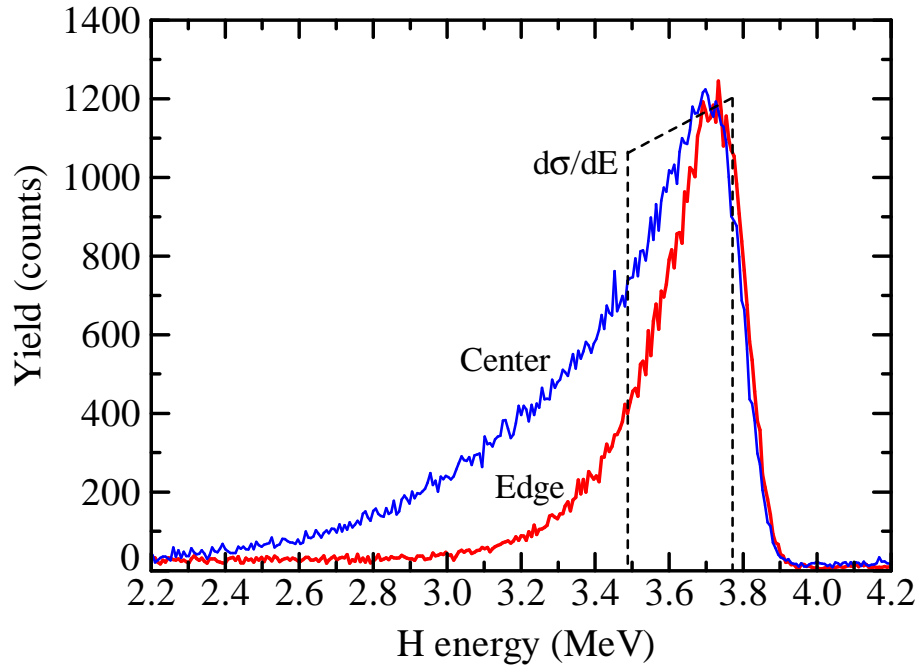


Figure 5: T-ERDA spectra for incidence of 8 MeV He on the center and edge of S-4 sample. In the latter case, less than about one-side half of the circular window of the detector is in the shadow of the sample holder, thereby low-energy H is selectively prevented from entering the detector. The calculated cross section $d\sigma/dE$ is also shown to have the same peak height.